Materials Research. 2023; 26: e20220370
DOI: https://doi.org/10.1590/1980-5373-MR-2022-0370

Microstructure and Mechanical Properties of Thick 08Cr9W3Co3VNbCuBN Heat-Resistant Steel welded Joint by TIP TIG Welding

Yongbin Wang[a], Peng Liu[a], Hongju Fan[a], Xinfang Guo[b], Fuwei Wan[b]*

[a]*Shandong Jianzhu University, School of Materials Science and Engineering, 250101, Jinan, P. R. China.*
[b]*Power China Nuclear Engineering Co., Ltd., 250102, Jinan, P. R. China.*

Received: August 18, 2022; Revised: March 20, 2022; Accepted: April 09, 2023

In this paper, the multi-layer multi-pass welding process was used to weld 115mm 08Cr9W3Co3VNbCuBN (G115) steel pipe, the gas tungsten arc welding (GTAW) was used in root pass welding, subsequent welding by dynamic hot wire gas tungsten arc welding (TIP TIG) welding method, while the post-weld heat treatment (PWHT) of 770°C × 10h was carried out afterward. The microstructure and mechanical properties of different zones of the welded joint were analyzed by OM, SEM, XRD, microhardness and impact tests. The results showed that the ferrite and martensite were observed in the weld metal (WM), the fine-grained heat-affected zone (FGHAZ) and the coarse-grained heat-affected zone (CGHAZ) consisting of prior austenitic grain boundaries (PAGBs) and martensite, and more precipitates including coarse $M_{23}C_6$ carbides with fine MX-type carbonitrides were observed inside the grain boundaries and grains. The hardness distribution patterns along different locations (Cover, Fill, Root) on the welded joint cross-section were the same, from base metal (BM) to WM hardness gradually increased, and WM hardness was the highest. WM impact toughness was worse than HAZ, impact fracture mode was a mixed tough-brittle fracture but biased towards brittle fracture.

Keywords: *G115 steel, multi-layer multi-pass, TIP TIG, precipitates, microstructure, mechanical property.*

1. Introduction

At present, 600°C ultra-supercritical (USC) power generation technology is widely used in thermal power plants around the world[1]. Thermal power generation meets the needs of people's life and also emits a large amount of CO_2, SOx, NOx, and other harmful gases, thus causing a great impact on the environment. To achieve the purpose of energy saving and emission reduction, the higher parameter ultra-supercritical thermal power units have gradually become the development direction of thermal power units[2,3]. The efficiency is improved by increasing parameters such as steam temperature and steam pressure of boilers in thermal power units, resulting in higher coal utilization, lower consumption, and consequently lower CO_2 emissions[4-6]. Currently, 9%-12% Cr martensitic heat-resistant steels are used as thick-section components in supercritical coal-fired power plants with steam temperatures of about 600°C because they have the advantages of high thermal conductivity, low coefficient of thermal expansion, low cost, and better thermal stability and excellent high-temperature durability compared with austenitic heat-resistant steels and nickel-based high-temperature alloys[7-10]. However, these conventional steels cannot break the maximum working temperature of 600°C[11], so it is necessary to develop high-temperature section heat-resistant steels.

In recent years, a novel martensitic heat-resistant steels have been developed worldwide based on the traditional martensitic heat-resistant steels P91 and P92, such as MarBN[12] and SAVE12AD[13] in Japan and IBN-1[14] in the UK. However, in China, G115 steel is the most promising candidate at 650°C. Unlike the above-mentioned steels, an appropriate amount of Cu is added to G115 steel to achieve a further increase in precipitation strengthening[15,16]. The steel has good organizational stability, excellent high temperature creep performance, better resistance to steam oxidation in the range of 630~650°C, its lasting strength at 650°C is 1.5 times that of P92 steel, and its resistance to high temperature steam oxidation and weldability is comparable to that of P92 steel. The steel can be used in the manufacture of thick-walled components such as large-diameter tubes and collectors, as well as small-diameter superheater and reheater tubes[17-20]. However, the application of G115 steel to key components of boilers in ultra-supercritical units at 630~650°C will inevitably involve welding. During the construction of coal-fired power plants and boiler installation, pipes and tubes are reliably connected by welding technology, so the performance of welded joints of high-temperature components of coal-fired power plants plays a key role in the safe and reliable operation of coal-fired power plants. Therefore, the quality of 9%-12% Cr martensitic heat-resistant steel welded joints is very important for the safe operation of coal-fired power stations.

Li et al.[21] welded dissimilar 9%Cr heat-resistant steels (G115 and CB2) by tungsten inert gas welding and studied the microstructure and mechanical properties of the welding metal. Maduraimuthu et al.[22], studied the effects of TIG and A-TIG welding processes on the microstructure and mechanical properties of P92 steel welded joints and confirmed that the precipitates at the grain and slab boundaries were

*e-mail: liupeng1286@163.com

$M_{23}C_6$ type carbides, and the precipitates in the grain were MX type niobium and vanadium rich nitrides and carbides. Cai et al.[23] successfully prepared a 15mm thick G115 welded joint by using the cold metal transition plus pulse (CMT+P) welding method, and studied the effect of heat input on the microstructure and mechanical properties of G115 steel welded joint. With the increase of heat input, the high-temperature duration of the welded joint increased, and the precipitation phase precipitated along the grain boundary and grain increased. Yang et al.[24] characterized the mechanical properties of G115/Sanicro25 dissimilar steel welded joints and studied the fine grain heat affected zone and base metal on the side of G115 steel. The results showed that FGHAZ on the G115 steel side had dynamic recovery after post-weld heat treatment, and the precipitates increased. However, the plates used for these jobs are around 15 mm, and thick plate G115 steel welding has not been reported.

To the author's knowledge, these welding operations were carried out on steel plates with a thickness of around 15 mm, necessitating an examination of the connection strategies for thick-walled pipes. However, partial fusion, poor impact performance, and damaging residual stresses were common with thick plate welding. Based on this, this paper examined a welding procedure that successfully joins 115 mm ultra-thick G115 pipes using gas tungsten arc welding (GTAW) + dynamic hot wire automation gas tungsten arc welding (TIP TIG)[25,26]. It also examined the microstructure and mechanical characteristics of the welded joints. As a result, our research encourages the future practical welding application of G115 heat-resistant steel and helps advance the creation of ultra-supercritical thermal power plants.

2. Experimental

2.1. Materials and welding process

The experimental material in this work was a G115 heat-resistant steel pipe of Φ530×115mm (115mm is the wall thickness). The BYH15 welding wire was trial produced by Beijing Beiye Functional Materials Co. Ltd. The wire diameter used for root pass welding was 2.4 mm and for subsequent filler welding was 1.0 mm. The chemical composition of materials was shown in Table 1. In this experiment, the gas tungsten arc welding (GTAW) was used for root pass welding, the dynamic hot wire gas tungsten arc welding (TIP TIG) was used for filler welding (see Figure 1). The groove of V type was selected, and the welding process and groove form were shown in Figure 2. The root surface and root space were 1.5mm and 3mm respectively. The number of weld layers was 48, and the number of weld beads was 179 (see Table 2). The welding process parameters were shown in Table 3, both the front shielding gas and the back shielding gas were argon gas, the gas flow rate of the front shielding gas was 10-15L/min, and the back shielding gas flow was 15~20L/min. The actual wire feeding speed can be expressed by the equation.

$$v = V \times a$$

Table 1. The chemical composition of G115 steel and BYH15 filler (wt.%).

Materials	C	Si	Mn	Cr	Ni	Al	Co
G115	0.07	0.34	0.58	8.82	0.03	0.002	2.99
BYH15	0.112	0.31	0.63	8.93	0.45	<0.01	2.97
Materials	Mo	W	V	B	Nb	N	Cu
G115	-	2.66	0.19	0.02	0.08	0.01	0.94
BYH15	<0.05	2.58	0.2	0.005	0.03	0.0023	-

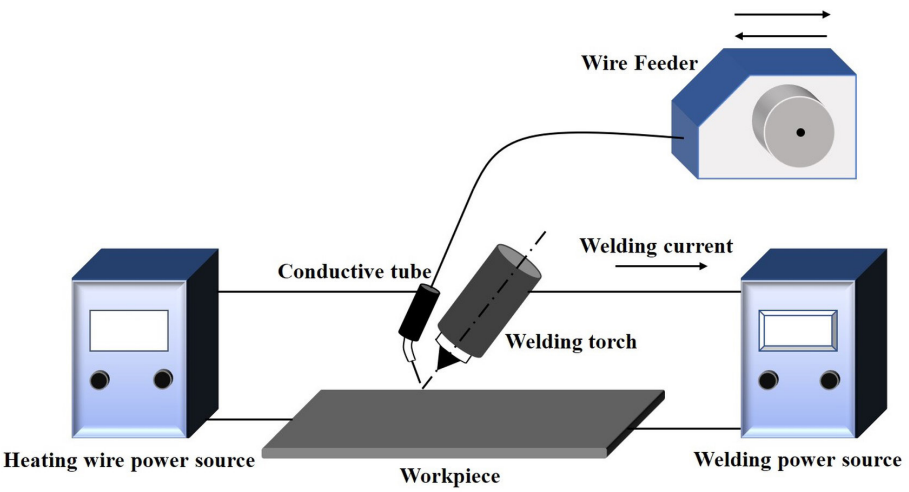

Figure 1. Schematic diagram of TIP TIG welding.

Table 2. The number of weld layers and weld beads.

Welding method	Weld layers	Weld beads
TIPTIG	48	6
TIPTIG	43-47	5
TIPTIG	14-42	4
TIPTIG	6-13	3
GTAW	5	3
GTAW	3-4	2
GTAW	1-2	1

Where v is actual wire feeding speed (m/min), V is the equipment setting parameter, the fill setting is 10-20, and the cover setting is 10-16. ^{a} is equipment factor (0.074). After calculation, the actual wire feeding speed is 0.74-1.18m/min and 0.74-1.48m/min (Table 3). As shown in Figure 3, the preheating temperature was maintained at 200°C. The interlayer temperature was maintained at 200~250°C during the welding process. After welding, the whole pipe weldment was subjected to post-weld heat treatment at 770 °C for 10h. This was a result of the wall of the G115 steel pipe was too thick, enough heat preservation time was required to ensure the effect of heat treatment.

Table 3. Welding process and parameters.

Region	Welding method	Wire diameter (ϕ)	Welding current (A)	Arc voltage (V)	Welding speed (mm·min-1)	Wire Feeding speed (m•min-1)
Cover	TIP TIG	1.0	150-180	11-15	50-80	0.74-1.18
Filling	TIP TIG	1.0	170-200	11-15	50-80	1.74-1.48
Root	GTAW	2.4	90-120	8-10	30-50	-

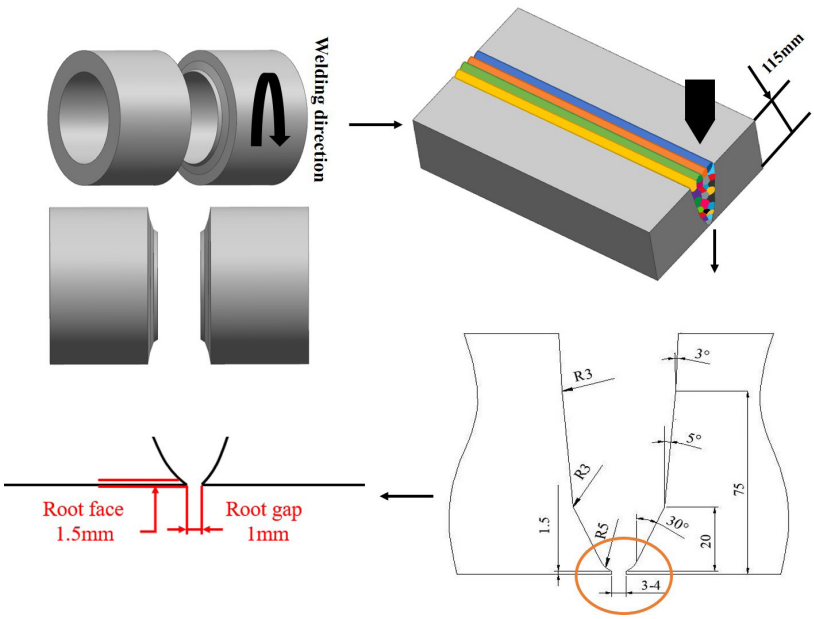

Figure 2. Schematic diagram of the welding heat treatment process.

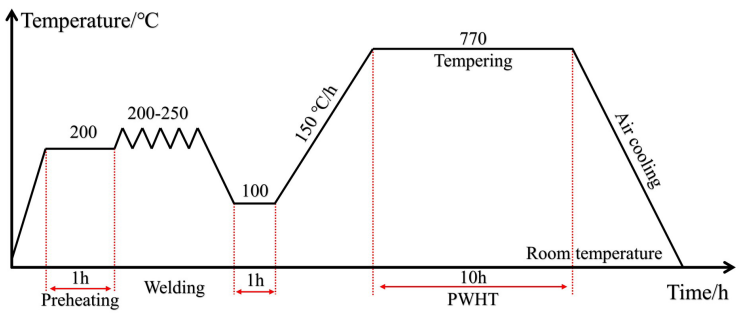

Figure 3. Schematic diagram of the welding process.

Nikon Epiphot 300U/200 horizontal metallographic microscope (OM), a Zeiss supraTM55 scanning electron microscope (SEM), energy dispersion spectrometer (EDS), and D/MAX-rc RU-200B X-ray diffractometer (XRD) were used to analyze the macrostructure and microstructure of the weld zone (WM) and the heat affected zone (HAZ). The samples were etched using mixed solution 5g $FeCl_3$ + 50ml HCl + 100ml H_2O. Hardness tests on the cross-sections region of the welds were performed using a Vickers Hardness Tester (DHV-1000) at room temperature for obtaining the hardness profiles in the WM, HAZ and base metal at a load of 0.02kg and dwell time of 10s.

The Charpy V-notch impact toughness test was carried out at room temperature. The test conformed to the NB47014/GB/T229 (20°C, KV2) standard (China). A sample with a size of 55mm×10mm×10mm was made for the impact test, as shown in Figure 4. The charpy V-notch impact test was carried out using a pendulum impact testing machine (JBW-300H type). The impact samples were respectively taken from the BM, the WM and the HAZ. The WM samples were taken from the positions shown in Figure 5a, and the HAZ samples were taken from Figure 5b.

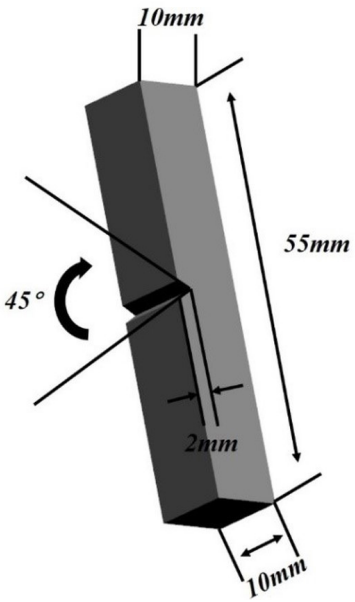

Figure 4. Schematic of impact shear test.

Three samples were taken from each position, and the average value was taken after the impact absorption energy was measured.

3. Results and Analysis

3.1. Microstructures

The macro-morphology of the G115 steel welded joint was shown in Figure 6. Due to the large sample, the corrosion effect was not ideal, but the joint was well formed. Due to the large depth of the weld, the welded joint was divided into upper, middle, and lower areas, which were the cover area, filling area, and root area respectively. In each area, heat affected zone and weld metal samples were prepared with a size of 10mm×10mm×10mm.

The microstructure of G115 base metal is shown in Figure 7. The main structure for the steel was lath martensite, which was more complex than that of austenitic steel. It was composed of original austenite grain, packet, block and lath. Several (3-5) martensitic lath packets with random orientation were in the prior austenite grain. Several parallel lath blocks were in the lath packet, several parallel martensitic laths were in the lath block, and a large number of dislocations existed in the lath. Each prior austenite grain was divided by these subunits, which were also called substructures. During tempering, numerous carbides ($M_{23}C_6$) were produced between the substructure, and these carbides could prevent the recovery and merger of the substructures of G115 steel during service, and stabilize the martensitic structure. In addition, two main strengthening phases existed in G115 steel including $M_{23}C_6$ carbide (M: Cr, Fe, W) and MX nitride (M: Nb, V, Cr; X: C, N). $M_{23}C_6$ carbide precipitates mainly along the prior austenite grain boundary, its existence hindered the slip of grain boundary, inhibited the recovery of lath martensite, and played a role in stabilizing the structure. The MX-type nitrides had fine particles, which played a dispersion strengthening effect on G115 steel, formed a pinning effect on the grain boundaries, and could achieve precipitation strengthening of the material by inhibiting the movement of dislocations.

The microstructure of the weld was shown in Figures 8, 9, and 10. According to the thermal effects of the welding process, perpendicular to the weld centerline direction, the welded joint had significant differences in the organizational characteristics of each region.

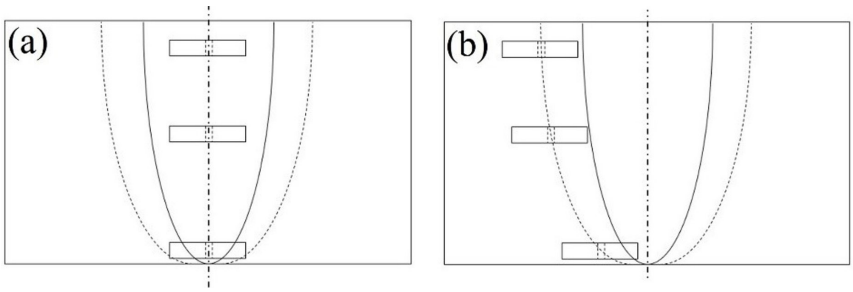

Figure 5. Schematic diagram of intercept position of impact sample: (a) WM, (b) HAZ.

The heat-affected zone was an important part of the welded joint, and because the heat-affected zone was far from the weld and absorbed different amounts of arc heat, the internal organization was extremely heterogeneous, which included the fine-grained heat-affected zone (FGHAZ) and the coarse-grained heat-affected zone (CGHAZ).

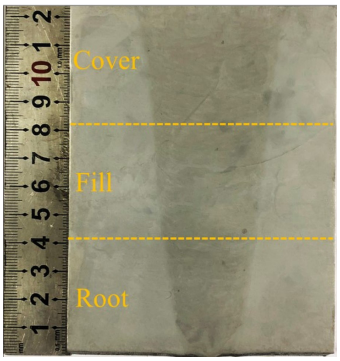

Figure 6. The structure in cross-sectional region for the G115 thick plate welded joint.

Figures 8, 9, and 10 showed the presence of prior austenitic grain boundaries (PAGBs) and lath martensite in both the FGHAZ and CGHAZ of the cap-filled zone, respectively. The temperature range of 1200-1300°C that CGHAZ experienced throughout the welding process[27], which was much higher than Ac3, led to complete austenitization. High temperatures in CGHAZ caused precipitation to dissolve, which eliminated their pegging impact. As a result, the pegging effect of these precipitations was lost. The rise in grain size was typical of CGHAZ because the dissolution of precipitates promoted grain growth and the consequent considerable growth of austenitic grains in this area. Lath martensite developed and nucleated inside the austenite grains as it cools, eventually creating PAGBs and lath martensite. The temperature experienced by FGHAZ was 1000-1100°C[27], and although it was higher than the critical temperature Ac3, the residence time of FGHAZ at this temperature was short and the temperature was not sufficient for coarse grain growth[23]. Because more undissolved precipitate pegging forces occurred on the grain boundaries and prevented the growth of austenite grains during welding, FGHAZ had smaller grains than CGHAZ.

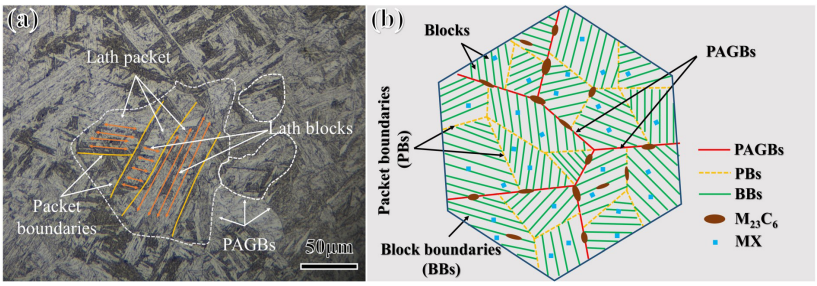

Figure 7. (a) The microstructure of base metal for G115 steel. (b) Schematic illustration of the microstructure of lath martensite and precipitated phase.

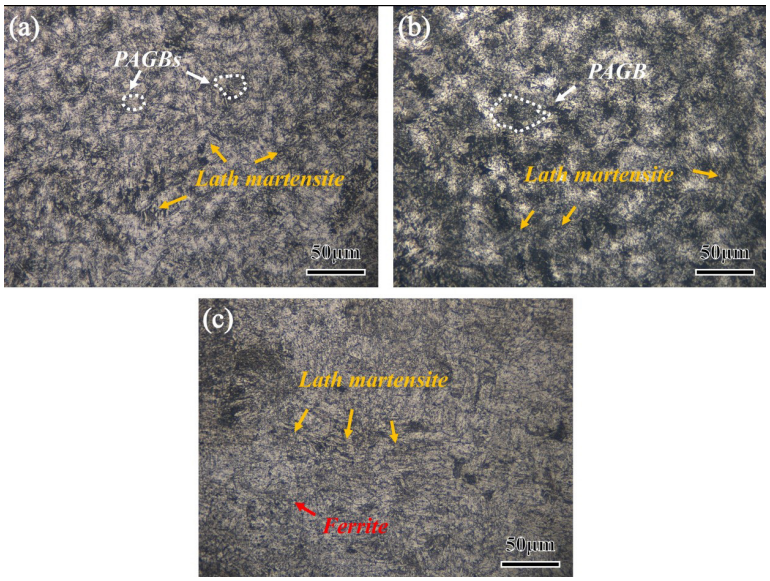

Figure 8. The microstructure in cover area of welded joint: (a) FGHAZ, (b) CGHAZ, (c) WM.

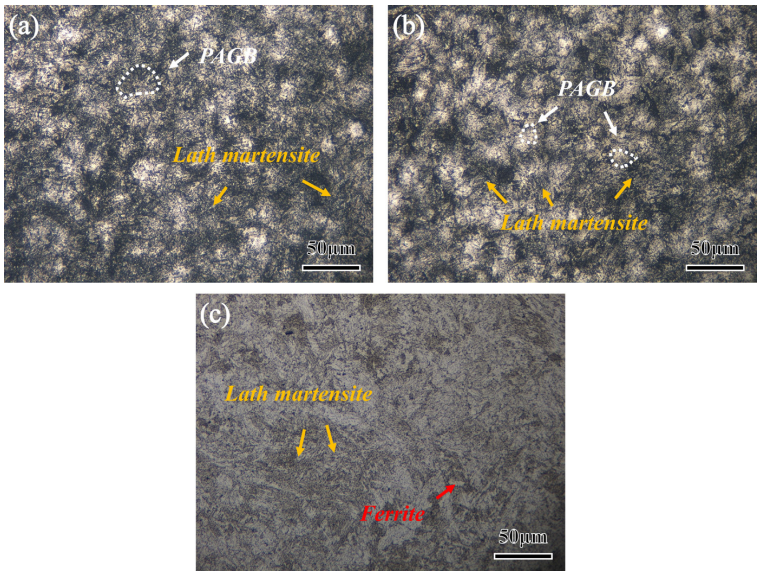

Figure 9. The microstructure in filling area of welded joint: (a) FGHAZ, (b) CGHAZ, (c) WM.

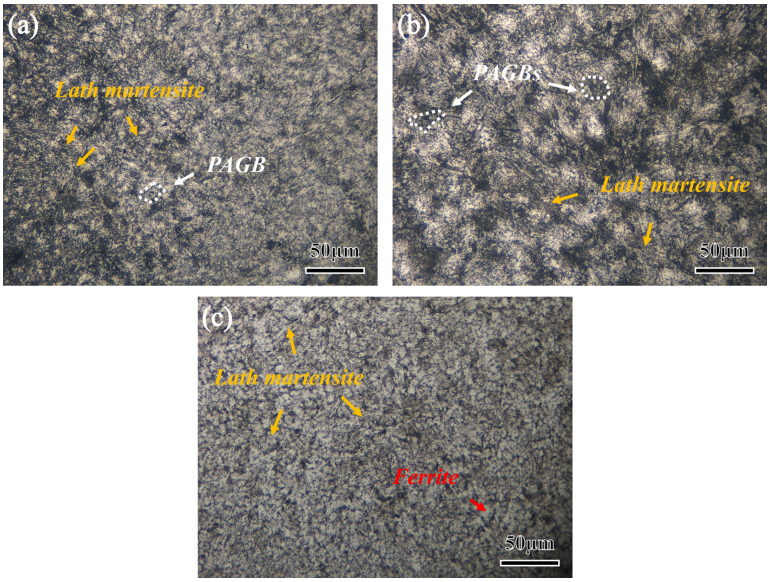

Figure 10. The microstructure in root area of welded joint: (a) FGHAZ, (b) CGHAZ, (c) WM.

The weld organization had two morphologies of equiaxed grains and columnar grains, the microstructure was composed of lath martensite, and ferrite was discovered. The weld metal also displayed a tempered martensitic structure. During the welding process, the coarse columnar grains grew in the direction opposite to the heat transfer, and the equiaxed grains were the result of the tempering effect of the next weld bead in the welding thermal cycle. From Figure 8c and 9c. It is obvious that the filler weld metal primarily had columnar grain martensite organization with different growth directions. This was caused by the high melt pool temperature and low base material temperature, which created a significant temperature gradient from the weld center to the base material as well as one between the weld bead center and the nearby area. Each temperature gradient caused a separate development direction for the liquid metal, which formed columnar grains.

As seen in Figure 10c, the weld root organization was primarily composed of equiaxed grain. This was due to two factors: (1) The first was the presence of just one weld bead at the weld root, which caused the grain to grow simultaneously from both sides of the base material to the weld center without showing any obvious columnar grain characteristics or only a few smaller-sized columnar grains. (2) Second, the filler layer had reheated the weld root, and a small number of columnar grains that were present during the subsequent welding operation were also changed into equiaxed grains.

3.2. EDS and XRD analysis

To further investigate the type of the above-mentioned large amount of precipitation in the FGHAZ of the root zone, EDS analysis was performed for the FGHAZ of the filled zone and root zone, as shown in Figure 11. From Figure 11a, it could be seen that the FGHAZ of the filled zone was rich in Fe and Cr, and contained a certain amount of Co and a small amount of W. The tissue composition was more uniformly distributed. However, FGHAZ in the root zone not only contained Fe, Cr, Co, and W, and contained V and C, as shown in Figure 11b. Elements V and C were the constituent elements of MX precipitation, which indicated that a large number of precipitation in the FGHAZ of the root zone contained MX precipitation, in the multi-layer multi-pass welding process each weld played a tempering effect which formed new $M_{23}C_6$ and MX precipitation, and in the post weld heat treatment increased the density of precipitation in the FGHAZ, a result that further verified the above-mentioned phenomenon of large amounts of precipitation in the FGHAZ of the root zone.

The results of the EDS analysis of the welded joints were shown in Figures 12, 13, and 14. From the plots with higher magnification, it could be seen that along the previous austenite grain boundaries (PAGB) there were some precipitates with a width of 200nm, which contained a large

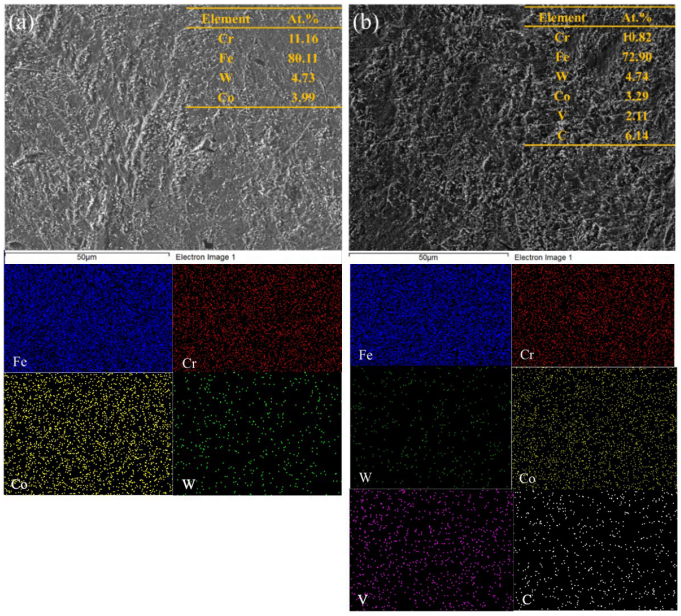

Figure 11. SEM observation and analysis in FGHAZ of welded joint: (a) Filling area, (b) Root area.

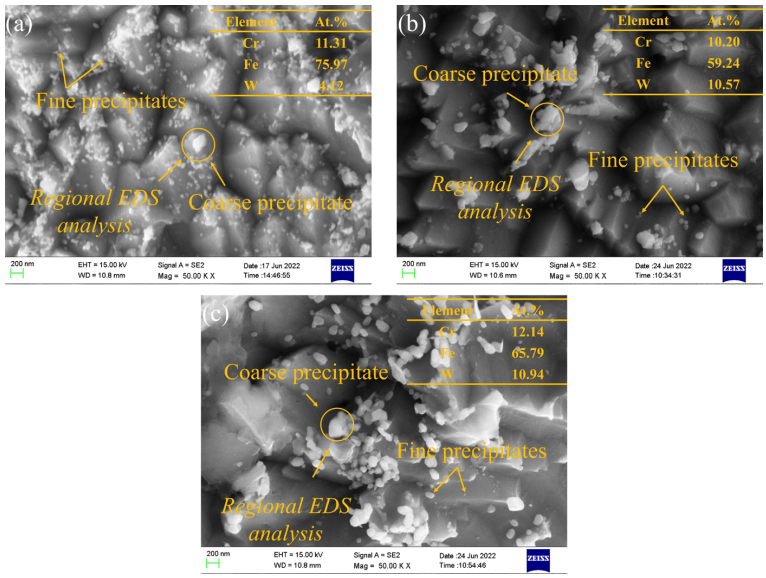

Figure 12. EDS analysis in FGHAZ of welded joint: (a) Cover area, (b) Filling area, (c) Root area.

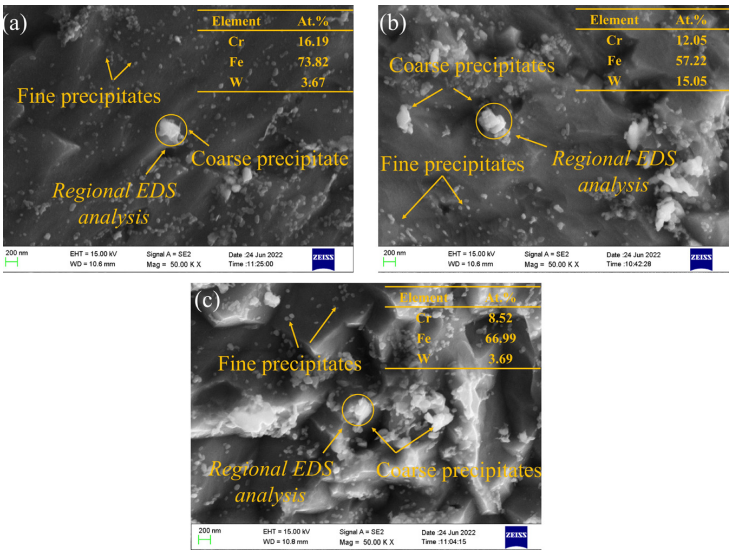

Figure 13. EDS analysis in CGHAZ of welded joint: (a) Cover area, (b) Filling area, (c) Root area.

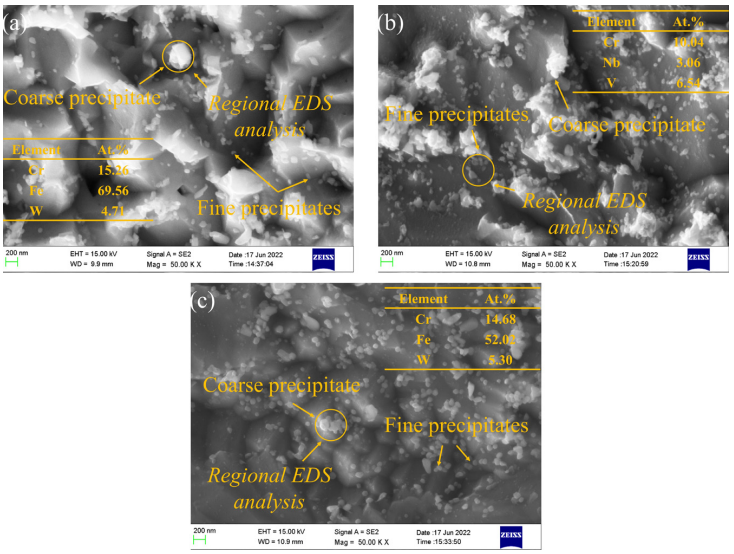

Figure 14. EDS analysis of the WM of (a) Cover area, (b) Filling area, (c) Root area.

amount of Fe and Cr and a small amount of W, as $M_{23}C_6$ precipitates. More minute precipitates were located inside the lath block, which contained Nb and V (see Figure 14b), as MX precipitates. During the welding process, each weld had a tempering effect on the previous weld that caused the precipitate content to increase significantly the longer it stayed at high temperatures. The smaller grain size of FGHAZ increased the grain boundary area compared to CGHAZ, which led to an increase in the location of the nucleation of the precipitated phase and an increase in the number of precipitated phases[22].

The phase composition of the HAZ and WM products were analyzed using XRD and the diffractograms were shown in Figure 15. The HAZ diffractograms (Figure 15a) showed peaks at $2\theta = 31.166°$, 44.675°, 65.026°, and 82.339° with the maximum intensity of the peak at 44.675°. The precipitation was identified by XRD analysis as V-rich MX particles and Cr- and Nb-rich $M_{23}C_6$ particles. The peak intensity at 31.166° confirmed the phases as VN and VC, the peak intensity at 44.675° confirmed the phases as α-Fe, $Cr_{23}C_6$, and VC, and the peak intensity at 65.026° confirmed the phases as αFe, $Cr_{23}C_6$, and VN, and the peak intensity at 65.026° confirmed the phases as α-Fe, $Cr_{23}C_6$, VC and NbN.

The XRD results in WM of welded joint (Figure 15b) showed peaks at $2\theta = 44.675°$, 65.026°, and 82.339°, with the maximum intensity of the peak at 44.675°. The precipitation was identified by XRD analysis as V-rich MX particles and Cr- and Nb-rich $M2_3C_6$ particles. The peak intensity at 44.675° confirmed the phases as α-Fe, $Cr_{23}C_6$, and VC, the peak intensity at 65.026° confirmed the phases as α-Fe, $Cr_{23}C_6$, and VN, and the peak intensity at 65.026° confirmed the phases as α-Fe, $Cr_{23}C_6$, VC and NbN.

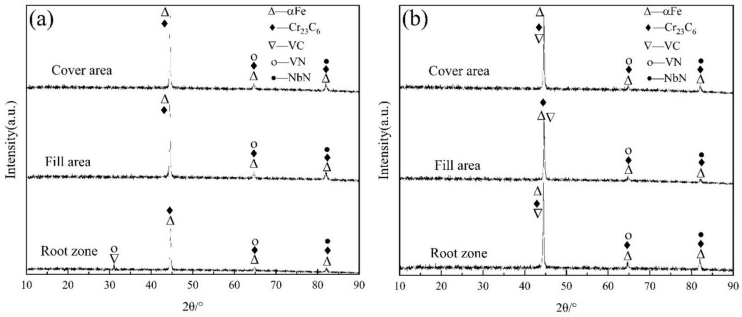

Figure 15. XRD patterns of different regions for welded joints: (a) HAZ, (b) WM.

Similar results were described by Zala et al.[28], who confirmed that the weld microstructure α-Fe phase of 9Cr-1Mo steel had three main peaks, similar to the base material. Saini et al.[29] determined by XRD analysis that P92 steel precipitates as Fe-rich Fe_3C, Nb- and V-rich MX particles, and Cr-rich $Cr_{23}C_6$, after creeping for 720h, the W-rich Fe_2W (Laves phase) was observed.

3.3. Mechanical properties

According to the test results, it could be observed that the hardness distribution pattern of the welded joint cross-sectional area was the same, from the base material to the weld area hardness gradually increased, and the weld area hardness was the highest, as shown in Figure 16. The difference between the hardness of the base material and the heat-affected zone was small. The hardness range of the base material was 220-240 HV0.2, with an average hardness of 229.6 HV0.2. The hardness range of the heat-affected zone was 240-260 HV0.2, with an average hardness of 248.9 HV0.2. And the hardness range of the weld zone was 260-300 HV0.2, with an average hardness of 280.7 HV0.2.

The highest hardness values in the WM were due to the presence of $M_{23}C_6$ carbide precipitated in the weld zone and its uniform distribution, which provided some reinforcement. The lower hardness values in WM were attributed to the presence of ferrite[30]. The average hardness of the HAZ was lower than that of the WM, but higher than that of the BM. This was due to the HAZ of the weld experienced thermal cycle and recrystallized, which was finer than the tempered martensitic grain of the base metal.

The impact test results were shown in Figure 17, the impact toughness of TIPTIG welds was lower than that of the base metal. Cai et al.[23] also reported the same results. Compared with Cold metal transfer plus pulse (CMT+P) welding, TIP TIG welding used in this work had better weld impact toughness. The impact test results show that the G115 pipe weldments obtained comply with the NB/T47014 standard (China) and the ASTM E23 standard for pressure equipment welding process assessment.

The impact fracture morphology in WM was shown in Figure 18, the V-notch location of the crack initiation zone was narrow, and the microscopic fracture of the crack initiation zone was mainly composed of dimples of different sizes and accompanied by deep holes, cracking dimples were generally composed of large particles of precipitates under the impact load to produce stress concentrations.

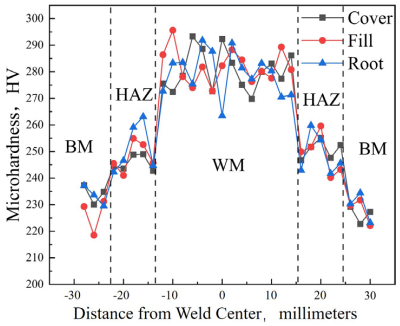

Figure 16. The hardness distribution profile of welded joint for G115 steel.

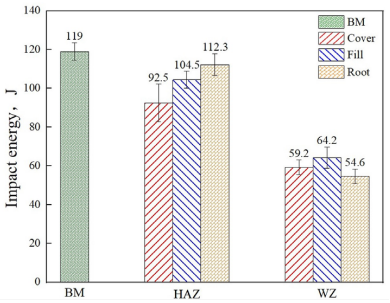

Figure 17. Charpy V-notch impact properties of welded joint for G115 steel.

The most dominant absorption region of the impact absorption energy was the crack initiation zone, which was very narrow in the fracture due to the low impact absorption energy, and the vast majority of the fracture was the extension zone. the pattern of the cleavage facets was a river pattern, consisting of smaller cleavage facets connected by a tearing ridge. The tear ridge had several dimple bands, whose flow direction coincides with the direction of crack expansion. Local presence of large smooth and cleavage facets with intergranular fracture. This was because the metal had inclusions or brittle precipitates that prevent plastic deformation. As a result, the material was unable to continue through the deformation to protect itself from damage and external force, and eventually along the crystal inside the particular crystal surface cracks and forms a cleavage fracture.

The impact fracture morphology in HAZ of welded joint was shown in Figure 19, which exhibited dimples of different sizes with holes. The cleavage facets with a river pattern were connected by a tear ridge with a large number of dimples. The fracture mode is a mixed tough-brittle fracture mechanism according to the fracture morphology.

It could be seen that the dimple size of the root zone of the weld and the HAZ was smaller than that of the filling zone and the covering zone. The filler layer would reheat the weld, which made the weld root structure undergo phase transformation and recrystallization in the subsequent welding process, the formation of self-tempering martensitic improved the plastic toughness of the weld metal. The small spherical second phase particles (the yellow circle) in the fracture of the sample were observed, it could be seen that these spherical second phase particles were one-to-one corresponding to the fear around them, indicating that a second phase particle was the nucleation position of a micro pit, determined that the second phase particles were MX nitrides combined with the literature[31-33].

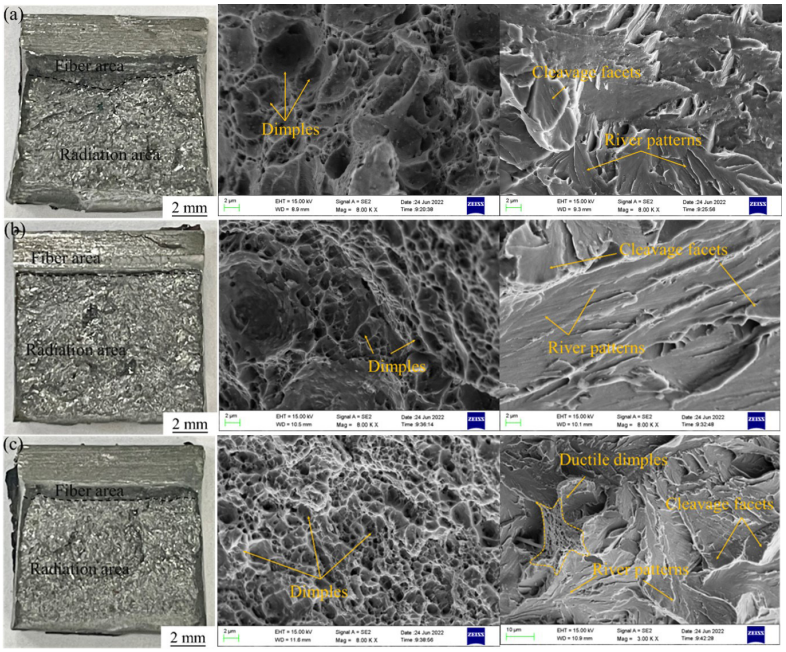

Figure 18. Impact fracture morphology in WM of welded joint: (a) Cover area, (b) Filling area, (c) Root area.

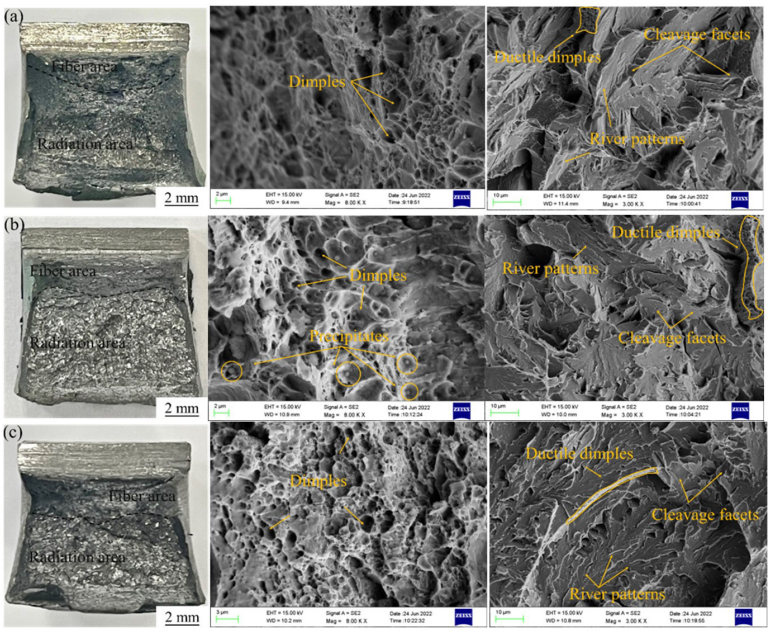

Figure 19. Impact fracture morphology in HAZ of welded joint: (a) Cover area, (b) Filling area, (c) Root area.

4. Conclusions

In this work, the welding process of GTAW +TIP TIG was used to achieve the welding of G115 thick-walled steel pipe and welding joints of good quality including no porosity and cracking were obtained. The microstructure of the welded joints was characterized by OM, SEM, XRD, and EDS. The mechanical properties of welded joints were studied by hardness and impact tests at room temperature. The following conclusions could be obtained:

(1) The microstructure of FGHAZ and CGHAZ consisted of prior austenitic grain boundaries (PAGBs) and lath martensite, with ferrite and martensite observed in the weld metal. A large number of precipitates were observed at the grain boundaries and inside the grains. The coarse precipitates precipitated along the grain boundaries were $M_{23}C_6$ carbides, and the fine precipitates precipitated inside the grains were MX-type carbonitrides.

(2) The EDS and XRD analysis showed that the G115 steel precipitates as α-Fe, $Cr_{23}C_6$, VC, VN and NbN in the joint were observed. In addition, the precipitation was identified by XRD analysis as V-rich MX particles and Cr- and Nb-rich $M_{23}C_6$ particles.

(3) The hardness distribution of welded joints was the same in different regions, however, from BM with an average hardness of 229.6 HV to WM (average 280.7 HV) gradually increased. The maximum hardness appeared in the WM of the joint fill, with a value of 297.7 HV. The impact absorbed energy of the WM was lower than that of the HAZ, while the average impact absorbed energy in the WM was 60.3J, and the average impact absorbed energy in the HAZ was 105.7J.

(4) The crack initiation zone of fracture was narrow, accompanied by dimples and holes, and most of the fracture area was the extension zone, accompanied by river pattern and deconstruction surface. The fracture morphology was analyzed as mixed tough-brittle fracture, but biased toward brittle fracture.

5. Acknowlegments

This work was financially supported by the Shandong Provincial Natural Science Foundation, China (Grant No. ZR2016JL017) and the Shandong Provincial Key Research and Development Program, China (Grant No. 2019TSLH0103).

6. References

1. Liu ZD, Cheng SC, Bao HS, Yang G, Gan Y, Xu SQ, et al. Research and development of advanced boiler steel tubes and pipes used for 600 °C USC power plants in China. Berlin: Springer; 2011. Advanced steels; p. 399-407.
2. Kostka A, Tak KG, Hellmig RJ, Estrin Y, Eggeler G. On the contribution of carbides and micrograin boundaries to the creep strength of tempered martensite ferritic steels. Acta Mater. 2007;552:539-50.
3. Xu YT, Li W, Wang MJ, Zhang XY, Wu Y, Min N, et al. Nano-sized MX carbonitrides contribute to the stability of mechanical properties of martensite ferritic steel in the later stages of long-term aging. Acta Mater. 2019;175:148-59.
4. Sklenicka V, Kucharova K, Svobodova M, Kral P, Dvorak J. The effect of a prior short-term ageing on mechanical and creep properties of P92 steel. Mater Charact. 2018;136:388-97.
5. Jin X, Zhu BY, Li YF, Zhao YF, Xue F, Zhang GD. Effect of the microstructure evolution on the high-temperature strength of P92 heat-resistant steel for different service times. Int J Press Vessels Piping. 2020;186:104131.
6. Masuyama F. History of power plants and progress in heat resistant steels. ISIJ Int. 2001;41:612-25.
7. Dudova N, Mishnev R, Kaibyshev R. Creep behavior of a 10%Cr heat-resistant martensitic steel with low nitrogen and high boron contents at 650 °C. Mater Sci Eng A. 2019;766:138353.
8. Rojas D, Garcia J, Prat O, Agudo L, Carrasco C, Sauthoff G, et al. Effect of processing parameters on the evolution of dislocation density and sub-grain size of a 12%Cr heat resistant steel during creep at 650°C. Mater Sci Eng A. 2011;528:1372-81.
9. Yin FS, Jung WS, Chung SH. Microstructure and creep rupture characteristics of an ultra-low carbon ferritic/martensitic heat-resistant steel. Scr Mater. 2007;57:469-72.
10. Gao QZ, Dong X, Li C, Lin ZX, Yang XX, Dai M. Microstructure and oxidation properties of 9Cr-1.7W-0.4Mo-Co ferritic steel after isothermal aging. J Alloys Compd. 2015;651:537-43.
11. Song YX, Ma Y, Chen HF, He ZB, Chen H, Zhang TH, et al. The effects of tensile and compressive dwells on creep-fatigue behavior and fracture mechanism in welded joint of P92 steel. Mater Sci Eng A. 2021;813:141129.
12. Guo J, Xu X, Jepson M, Thomson RC. Influence of weld thermal cycle and post weld heat treatment on the microstructure of MarBN steel. Int J Press Vessels Piping. 2019;174:13-24.
13. Hamaguchi T, Okada H, Kurihara S, Hirata H, Iseda A. Microstructural evaluation of 9Cr-3W-3Co-Nd-B heat-resistant steel (SAVE12AD) after long-term creep deformation. In: ASME 2017 Pressure Vessels and Piping Conference; 2017; Waikoloa, Hawaii, USA. Proceedings. New York: ASME; 2017.
14. Zhang Z, Mee VVD, Allen D. Assessment of deposit microstructure and all-weld and joint creep performance of the matching filler metal for the MARBN alloys. Mater High Temp. 2021;38:342-50.
15. Xiao B, Xu L, Tang Z, Zhao L, Jing H, Han Y, et al. A physical-based yield strength model for the microstructural degradation of G115 steel during long-term creep. Mater Sci Eng A. 2019;747:161-76.
16. Xiao B, Xu LY, Cayron C, Xue J, Logé R. Solute-dislocation interactions and creep-enhanced Cu precipitation in a novel ferritic-martensitic steel. Acta Mater. 2020;195:199-208.
17. Yamamoto Y, Ortolani M. Micrograin structure evolution associated with grain boundary characteristics in grade 91 steel during long-term creep exposure. Mater Sci Eng A. 2021;826:141993.
18. Fedoseeva A, Dudova N, Kaibyshev R. Creep strength breakdown and microstructure evolution in a 3%Co modified P92 steel. Mater Sci Eng A. 2016;654:1-12.
19. Guo S, Zhang W, Yin P, Ma TH, Wen JB, Zhang GD, et al. Cyclic deformation behavior and life prediction of P92 steel welded joints under thermomechanical fatigue loadings. Int J Fatigue. 2021;147:106183.
20. Liu Z, Wang XT, Dong C. Effect of boron on G115 martensitic heat resistant steel during aging at 650 °C. Mater Sci Eng A. 2020;787:139529.
21. Li T, Yuan XJ, Li R, Xiong JK, Tao SW, Wu KL. Microstructure and mechanical characteristics of dissimilar TIG welded 9% Cr Heatresistant steels joints. Int J Precis Eng Manuf. 2021;22:1007-19.
22. Maduraimuthu V, Vasantharaja P, Vasudevan M, Panigrahi BS. Microstructure and mechanical properties of 9Cr-0.5Mo-1.8W-VNb (P92) steel weld joints processed by fusion welding. Mater Sci Eng A. 2021;813:141186.
23. Cai HY, Xu LY, Zhao L, Han YD, Pang HN, Chen W. Cold metal transfer plus pulse (CMT+P) welding of G115 steel: Mechanisms, microstructure, and mechanical properties. Mater Sci Eng A. 2022;843:143156.

24. Yang MH, Zhang Z, Liu YR, Li LP, Huang JK. Fine-grain heat affected zone softening of G115/Sanicro25 dissimilar steel welded joints after post-weld heat treatment. Int J Press Vessels Piping. 2020;188:104253.
25. Madsen O, Wilson M. TIP TIG: new technology for welding. Ind Rob. 2007;34:462-6.
26. Wang LL, Zhao PC, Pan JJ, Tan L, Zhu KX. Investigation on microstructure and mechanical properties of double-sided synchronous TIP TIG arc butt welded duplex stainless steel. Int J Adv Manuf Technol. 2021;112:303-12.
27. Dak G, Pandey C. Experimental investigation on microstructure, mechanical properties, and residual stresses of dissimilar welded joint of martensitic P92 and AISI 304L austenitic stainless steel. Int J Press Vessels Piping. 2021;194:104536.
28. Zala AB, Jamnapara NI, Sasmal CS, Sam S, Ranjan M. Study of microstructure & mechanical properties of TIG welded aluminized 9Cr-1Mo steel. Fusion Eng Des. 2022;176:113038.
29. Saini N, Mulik RS, Mahapatra MM. Study on the effect of ageing on laves phase evolution and their effect on mechanical properties of P92 steel. Mater Sci Eng A. 2018;716:179-88.
30. Liu X, Lu FG, Yang RJ, Wang P, Xu XJ, Huo X. Investigation on Mechanical Properties of 9%Cr/CrMoV Dissimilar Steels Welded Joint. J Mater Eng Perform. 2015;24:1434-40.
31. Deng D, Murakawa H. Numerical simulation of temperature field and residual stress in multi-pass welds in stainless steel pipe and comparison with experimental measurements. Comput Mater Sci. 2006;37:269-77.
32. Sakthivel T, Vasudevan M, Laha K, Parameswaran P, Chandravathi KS, Selvi SP. Maduraimuthu, Mathew M D. Creep rupture behavior of 9Cr-1.8W-0.5Mo-VNb (ASME grade 92) ferritic steel weld joint. Mater Sci Eng A. 2014;591:111-20.
33. Pandey C, Mahapatra MM, Kumar P, Saini N. Effect of Normalization and Tempering on Microstructure and Mechanical Properties of V-Groove and Narrow-groove P91 Pipe Weldments. Mater Sci Eng A. 2017;685:39-49.